Molecular simulation and experimental investigation of CO2 capture in a polymetallic cation-exchanged 13X zeolite

Chen, S., Zhu, M., Tang, Y., Fu, Y., Li, W., & Xiao, B. (2018). Molecular simulation and experimental investigation of CO2 capture in a polymetallic cation-exchanged 13X zeolite. *Journal of Materials Chemistry A*, *6*(40), 19570-19583. https://doi.org/10.1039/C8TA05647A

Published in:
Journal of Materials Chemistry A

Document Version:
Peer reviewed version

Queen's University Belfast - Research Portal:
Link to publication record in Queen's University Belfast Research Portal

Molecular simulation and experimental investigation of CO_2 capture in a polymetallic cation-exchanged 13X zeolite

Shujun Chen[a,b,*], Min Zhu[a], Yingchun Tang[c], Yue Fu[a], Wenliang Li[a] and Bo Xiao[d]

ABSTRACT: There is a great need to synthesize high-performance adsorbents for potential application in post-combustion CO_2 capture. In this study, molecular simulation was employed to mimic cation exchanges in 13X zeolite with different amounts of Li^+, K^+, and Ca^{2+}, providing guidance for the design of high-performance cation-exchanged zeolite. The separation performance of each cation-exchanged zeolite was evaluated in detail in terms of its pore volume, CO_2 adsorption capacity, regeneration performance, and CO_2/N_2 selectivity. The simulated results showed that the fresh LiX-80 zeolite sample was the most promising adsorbent for CO_2/N_2 separation. On this basis, a novel polymetallic cation-exchanged zeolite was developed by introducing Pd^{2+} and Ag^+ into the LiX-80 (LiPdAgX). LiPdAgX exhibited a more CO_2 loading and higher CO_2/N_2 selectivity than 13X and LiX-80 zeolites. Finally, adsorption experiments were performed on the 13X, LiX, and LiPdAgX zeolites, and the simulations agreed well with the experimental results. This study provides microscopic-level insights into gas adsorption and separation in polymetallic cation-exchanged zeolites, and suggests that LiPdAgX zeolite can effectively enhance CO_2 capture.

***Keywords*:** 13X zeolite, CO_2 capture, Molecular simulation, Cation-exchange, Selectivity

1. Introduction

The issue of anthropogenic climate change driven by greenhouse gas emissions is attracting increasing concern. Replacing fossil fuels with clean energy sources is one solution for reducing CO_2 emissions. However, optimizing the structure of existing energy sources is difficult in the short-term. Therefore, the capture of CO_2 in order to prevent the predicted global increase in temperature is proposed by some as a medium-term solution until the wide-scale use of renewables as the primary source of energy becomes viable.[1] According to the International Energy Agency (IEA), appropriate CO_2 capture and storage (CCS) has the potential of decreasing CO_2 emissions up to 20%.[2]

There are many CO_2 capture technologies available, including chemical absorption, physical adsorption, membrane and cryogenic separation.[3] Owing to their high CO_2 uptake, low energy consumption, and non-toxic nature, adsorption technologies are among the most effective methods of CO_2 capture. Recently, many different solid adsorbents, such as activated carbon,[4] zeolite,[5] metal-organic frameworks (MOFs),[6] organic-inorganic hybrid/composite adsorbents,[7] porous polymers,[8] carbon nanotubes,[9] and silicon carbide,[10] have been used to capture CO_2. Among the

[a] *College of Pipeline and Civil Engineering, China University of Petroleum (East China), Qingdao 266580, China.*

[b] *Shandong Key Laboratory of Oil & Gas Storage and Transport Safety, Qingdao 266580, China.*

[c] *Sino German Institute of Shenyang Polytechinic College, Shenyang 110045, China.*

[d] *School of Chemistry and Chemical Engineering, Queen's University Belfast, Belfast BT9 5AG, UK.*

[*] Corresponding author: E-mail address: shujunchenfu@126.com (S.J. Chen).

porous adsorbents, zeolite has traditionally been the most widely-used option, due to its low cost, good availability, large surface area, porous texture, high CO_2 adsorption capacity, fast kinetics, and good chemical and thermal stability.[11-16]

The development of a material that features a lower energy penalty for regeneration, while maintaining high CO_2 adsorption capacity and selectivity over the other components in the flue gas, is crucial for improving the commercial viability of CCS. To improve the CO_2 adsorption capacity and selectivity for CO_2 adsorption over N_2 in flue gases, a series of alkali cation (Li, Na, K, Cs and Rb) and alkaline-earth cation (Mg, Ca and Sr,) exchanged samples of a new zeolite were studied.[17-24] The results have demonstrated that the adsorption capacity and CO_2/N_2 selectivity of zeolite can be significantly changed after undergoing cation-exchange. The type of extra framework cation has a profound influence on the pore volume and CO_2 adsorption characteristics of the zeolite.[17,18] The strong coulombic interactions of CO_2 with extra-framework cations result in strong binding and selective capture.[19] The CO_2 capture capacity of zeolite is strongly dependent upon the ionic radii, cation concentration and electropositive character, and the CO_2 loading amount.[20-22] In addition to the above metal cations, small amounts of precious metal cations, such as Ag^+ and Pd^{2+}, were exchanged to the zeolites.[25-30] the adsorption of ethylene on a series of Ag^+ exchanged zeolites was investigated.[25,26] they have found that the key element in the adsorption for Ag^+ exchanged zeolites is the formation of the stable π-complexes of ethylene with Ag^+. The Ag^+ exchanged X zeolites have higher N_2/O_2 selectivity and adsorption capacity of N_2. This is due to the weak-complexation bond similar to that between ethylene and Ag^+.[27,28] The studies of Pd^{2+} and Ag^+ exchanged zeolite are mostly on catalyst because of the high activity of Pd and Ag in various important catalytic processes. T. Frising et al.[29] have reported the preferred sites for the distributions of Ag^+ and Pd^{2+} in X and Y faujasite zeolites. O. Terekhina et al.[30] have used CO adsorption to probe electronic properties and the surface properties of the Pd-Ag cation-exchanged zeolite. On addition of Ag^+ to Pd^{2+}, CO molecules experience an electronic environment that is different from that of the monometallic sample, CO adsorption can pull strongly binding Pd atoms to the surface. Furthermore, adding Ag^+ can increase the stability of the Pd^{2+} cluster during the CO adsorption due to the electron density transfer from Ag to Pd. As reviewed above, the combination of Ag^+ and Pd^{2+} may be of benefit to the adsorption capacity and selectivity. In this study, to develop a novel, more efficient adsorbent for CO_2 capture, based on the 13X zeolite which is one of the best performing zeolites for CO_2 adsorption,[31,32] a pinch of Pd^{2+} and Ag^+, and large amounts of Li^+ were exchanged into 13X zeolite to create a polymetallic cation-exchanged 13X zeolite.

While the preparation of zeolite with different cations and exchange degrees can be high cost, and the experimental evaluation of their adsorption performance is tedious and time consuming,

particularly for gas mixtures. As an important complement to experiments, molecular simulation such as Grand Canonical Monte Carlo (GCMC) and Molecular Dynamics (MD), have been used to guide experimental efforts to screen large libraries of material,[33,34] provide microscopic mechanism of adsorption behavior,[35-37] as well as guide for the design of high-performance cation-exchanged microporous materials.[23,38]

In this study, molecular simulations were used to develop a novel polymetallic cation-exchanged 13X zeolite for potential application in post-combustion CO_2 capture. Firstly, 13X was used as the precursor, and different amounts of Li^+, K^+, and Ca^{2+} were then introduced into it respectively. The separation performance of the cation-exchanged zeolite was evaluated in detail by measuring its pore volume, CO_2 adsorption capacity, regeneration performance, and CO_2/N_2 selectivity. Sample LiX-80, which contained 80 Li^+, exhibited the best separation performance. Following, a pinch of Pd^{2+} and Ag^+ were added to the LiX-80 zeolite, creating a polymetallic cation-exchanged zeolite that was named "LiPdAgX". The best performing LiPdAgX from CO_2 loading, CO_2/N_2 selectivity and average adsorption energy is directly compared with LiX-80. The microscopic mechanism of the adsorption separation effect of metal cations on zeolite was also explored. Finally, adsorption experiments were performed on the 13X, LiX, and LiPdAgX zeolites, and the results of the experiments were compared with the simulated results.

2. Molecular simulation methods

2.1 X zeolite model

13X zeolite belongs to one of the FAU-type zeolite. FAU is a mineral group in the zeolite family and X is a type of FAU zeolite for a Si/Al ratio within a low range of 1 to 1.5. The zeolite framework was built with the Si/Al ratio 1.23 in accordance with the Lowenstein's Al–O–Al avoidance rule,[23] and it has a dehydrated composition of $Na_{86}Al_{86}Si_{106}O_{384}$ with a lattice parameter of 2.5028 nm and angles of 90°.[39,40] The simulation model of 13X zeolite is shown in Fig.1. The partial charges of the atoms in the skeleton for 13X zeolite were calculated in our previous study, as listed in Table 1.[40]

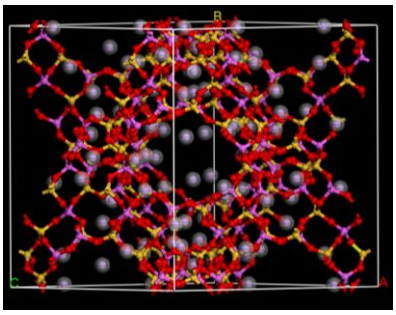

Fig.1. Simulated model of 13X zeolite. Key: red= O; yellow= Si; purple= Al; grey= Na.

Table 1 Partial charges of 13X zeolite

Atom	O	Si	Al	Na
Charge/e	-0.359	0.26	0.713	0.57

The 13X zeolite was modified by exchanging metallic cations, including Ca^{2+}, K^{+}, and Li^{+}, with the Na^{+} ions in the zeolite. A study on the modification of X zeolite demonstrated that the exchange degree of Na^{+} in X zeolite can reach 99.95%.[41] In this range, 72, 76, and 80 Na^{+} were replaced with Li^{+}, K^{+}, and Ca^{2+}, respectively. The metallic cation-exchanged 13X zeolites are herein referred to as LiX-72, LiX-76, LiX-80, KX-72, KX-76, KX-80, CaX-36, CaX-38, and CaX-40. The microstructure information of these materials was obtained using Materials Studio (MS) software.

2.2 Adsorbates: CO_2 and N_2

The molecular models of CO_2 and N_2 are depicted in Fig.2. CO_2 and N_2 were modelled as triatomic molecules, with CO_2 containing a C atom in the centre and two O atoms at both ends, and N_2 containing a fictional zero-mass atom in the centre and two N atoms at both ends.[42] CO_2 is taken to be rigid, with a C-O double bond, length of 1.179 Å,[40] a quadrupole moment of 4.30×10^{-26} esu cm^2,[43] a polarizability of 26.5×10^{-25} cm^3,[43] and charges of +0.72 and -0.36 e on the C and O atoms, respectively.[40] Although N_2 is actually a diatomic molecule, a fictional zero-mass site is added to the molecule so that a quadrupole could be modeled with an overall neutral charge. N_2 is taken to be linear and rigid, with a triple N-N bond length of 1.098 Å,[40] a quadrupole moment of 1.52×10^{-26} esu cm^2,[43] a polarizability of 17.6×10^{-25} cm^3,[43] and charges of +0.964 and -0.482 e on the fictional zero-mass and N atoms, respectively.[44]

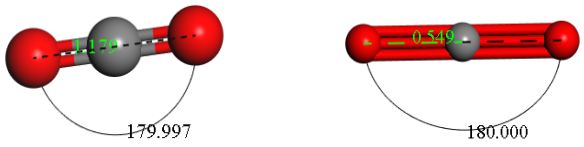

(a) CO_2. Key: red= O; grey= C. (b) N_2. Key: red= N; grey= fictional zero-mass atom.

Fig.2. Molecular models of (a) CO_2 and (b) N_2.

2.3 Force field parameters

The universal force field (UFF) was used during each simulation process. The Ewald summation method with accuracy 0.004 kJ mol^{-1} and the atom-based summation method were respectively applied to the electrostatic terms and the van der Waals term, and the cutoff radius of which was 12 Å.[45] The interactions between CO_2 and N_2 molecules and the atoms in zeolite are described by a combination of the Lennard-Jones (LJ) and Columbic potentials:[35,40,46,47]

$$u_{LJ} = \sum_{i,j} \sum_{i \neq j} 4\varepsilon_{ij} \left(\left(\frac{\sigma_{ij}}{r_{ij}} \right)^{12} - \left(\frac{\sigma_{ij}}{r_{ij}} \right)^{6} \right) + \frac{q_i q_j}{4\pi\varepsilon_0 r_{ij}} \quad (1)$$

where r is the distance between the centers of two interacting sites of typs i and j, σ is the site diameter, ε is the depth of the potential well, q is the partial charge applied to each site, and ε_0 is the vacuum permittivity (8.85419×10^{-12} C^2 $J^{-1}m^{-1}$).

There are a variety of metal elements in the modified zeolite, so it was simulated using UFF, which covers all elements in the periodic table. The Lorentz-Berthelot combining rules of $\sigma_{ij} = (\sigma_i + \sigma_j)/2$ and $\varepsilon_{ij} = \sqrt{\varepsilon_i \varepsilon_j}$, respectively, were used to calculate the LJ interactions between adsorbent and adsorbates.[47,48] The LJ potential parameters for all the atoms of adsorbate and adsorbent based on UFF was shown in Table 2 from MS software.

Table 2 LJ parameters used in the adsorption simulation

atom	σ/ Å	ε/ (kJ mol^{-1})
O	3.5000	0.2510
C	3.8510	0.4393
N	3.6600	0.2887
Si	4.2950	1.6820
Al	4.4990	2.1129
Na	2.9830	0.1255

2.4 Simulation methodology and details

In 13X zeolite and each metallic cation-exchanged zeolite, the adsorptions of pure CO_2 and N_2, as well as CO_2/N_2 binary mixture, were simulated at a temperature of 298 K and pressures ranging from 0 to 1500 kPa using GCMC simulation method. The adsorption capacities of each gas component were calculated by specifying the bulk pressure, temperature, and compositions of the bulk gas mixture during GCMC simulation. The periodic boundary conditions were exerted during all simulations. Metropolis Monte Carlo methods were then followed, including trials of creation, destruction, regrowth, rotation, and translation. There were 3×10^6 trial moves in a typical GCMC simulation; the first 1.5×10^6 moves were used for equilibration and the subsequent 1.5×10^6 moves were used to determine ensemble averages.

2.5 Adsorption isotherms

The relationship between pressure, temperature and uptake of an adsorbate-adsorbent system is known as the adsorption equilibrium model. The pure CO_2 isotherms obtained from the GCMC

simulations were fitted to the dual-site Langmuir model, which is expressed by Eq. (2-4):

$$n = \frac{n_1 K_1 p}{1 + K_1 p} + \frac{n_2 K_2 p}{1 + K_2 p} \quad (2)$$

$$K_1 = b_1 \exp\left(\frac{Q_1}{RT}\right) \quad (3)$$

$$K_2 = b_2 \exp\left(\frac{Q_2}{RT}\right) \quad (4)$$

where n is the loading; p is the equilibrium pressure; T is the temperature; n_1 and n_2 are the saturated adsorption capacity values corresponding to sites 1 and 2, respectively; Q_1 and Q_2 are adsorption heat values at sites 1 and 2, respectively; R is the universal gas constant; K_1 and K_2 are the gas adsorption equilibrium constant at active sites 1 and 2, respectively; and b_1 and b_2 represent the equilibrium constant of adsorption when the temperature tends to infinity.

2.6 Isosteric heat of adsorption

The Clapeyron–Clausius equation is commonly used to estimate the heat of adsorption at constant concentrations which is given by Eq. (5). The isosteric heat of adsorption, Q_{st}, is defined as:

Commented [陈1]: 这里应是方程（4）还是（5）？

$$Q_{st} = RT^2 \left(\frac{\partial \ln p}{\partial T}\right)_n \quad (5)$$

2.7 The adsorption Energy

The adsorption energy (E_{ad}) of the gas in a zeolite can be calculated as:

$$E_{ad} = E_{z+a} - E_z - E_a \quad (6)$$

where E_z is the total energy of optimised zeolite unit, E_a is the total energy of the gas molecule, and E_{z+a} is the total energy of the zeolite/gas molecule system at equilibrium. Adsorption energy is important for measuring the regeneration performance of zeolite, and E_{ad} is negative because the adsorption process is exothermic. A higher negative value of E_{ad} reflects that the zeolite needs higher temperatures to regenerate.

2.8 The adsorption selectivity

With regard to the separation process, the most interesting and important parameter is the selectivity ($S_{i/j}$). For mixtures, the CO_2/N_2 selectivity is important for CO_2 capture from a mixture of CO_2/N_2. This is defined as follows:

$$S_{i/j} = \frac{\left(x_i / y_i\right)}{\left(x_j / y_j\right)} \quad (7)$$

where x_i, x_j, y_i, and y_j denote the molar fraction of components i and j in the adsorptive and bulk adsorbate phases, respectively. A selectivity of $S_{i/j}>1$ indicates preferential adsorption for

component *i* over component *j* in the binary mixture. The interactions between gas molecules and zeolite are mainly controlled by van der Waals force and electrostatic force, so the electrostatic potential (ESP) has an important influence on the gas adsorption, especially in the separation of mixed gas with large difference in quadrupole moments. The ESP (V) at a given point (r) in the space around the molecule can be expressed as:

$$V(r) = \sum_A \frac{Z_A}{|R_A - r|} - \int \frac{\rho(r')dr'}{|r - r'|} \quad (8)$$

where Z_A is the charge of nucleus A and $\rho(r')$ is the electron density of molecules. The sign of $V(r)$ in any region is determined by whether the positive contribution of the nuclei or the negative contribution of the electrons. The ESP calculations were performed using the general gradient approximate density functional[49-51] and double numerical (DN) plus d-functions (DN with a polarisation d-function was used here for all non-hydrogen atoms, which is a viable alternative to ab initio methods and can provide reasonable accuracy for computation). The cross-correlation energy was determined using Hamprecht, Cohen, Tozer and Handy functional.

3. Simulation results and discussion

3.1 Microstructure information

3.1.1 Phase analysis

To validate the reliability of the 13X zeolite model and feasibility of the simulated method, the simulated X-ray diffraction (XRD) pattern was compared to that from experimental data[52], as shown in Fig.3 and Table 3. In Fig.3, the characteristic peak positions in the simulation result and the experimental data were almost identical. Crystalline phases were identified by comparison with standard reference patterns from Powder Diffraction File PDF-2 database sets 1-45, which is maintained by the International Centre for Diffraction Data. The phase on the crystallographic plane index of 111 is $Na_2Al_2Si_{2.5}O_9 \cdot 6.2H_2O$, which is a typical 13X zeolite structure. Table 3 lists the characteristic peak positions for the simulated result, experimental data, and standard reference pattern for 13X zeolite. The errors of 2θ at the crystallographic plane indices of 111, 220, 311, and 331 between the simulated result and experimental data, and the reference patterns are very small (< 0.1). These analyses indicate that the 13X zeolite model presented here is reliable, and that the simulation method used to obtain the XRD pattern is feasible and accurate.

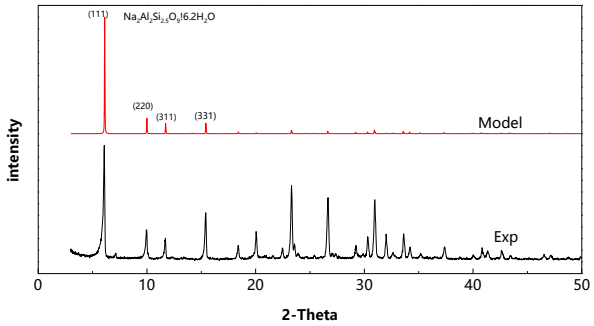

Fig.3. Comparison of the XRD patterns for the 13X zeolite model with the experimental result.

Table 3 Diffraction angles for the characteristic peak of the main crystallographic planes in13X zeolite

Crystallographic	2θ/°		Criterion of 2θ	Error	
plane index	Model	Experiment	/°	Model	Experiment
（111）	6.122	6.076	6.103	0.019	-0.027
（220）	10.074	9.943	9.986	0.088	-0.043
（311）	11.721	11.694	11.727	-0.006	-0.033
（331）	15.499	15.384	15.451	0.048	-0.067

The XRD patterns for LiX, KX, and CaX zeolites models were illustrated in Fig.4. All samples exhibit characteristic peaks of X zeolites with no other impurity phases, representing that the metallic cation-exchange of 13X zeolites can't destroy the framework. The characteristic peak positions are nearly identical for LiX, KX, and CaX zeolites.

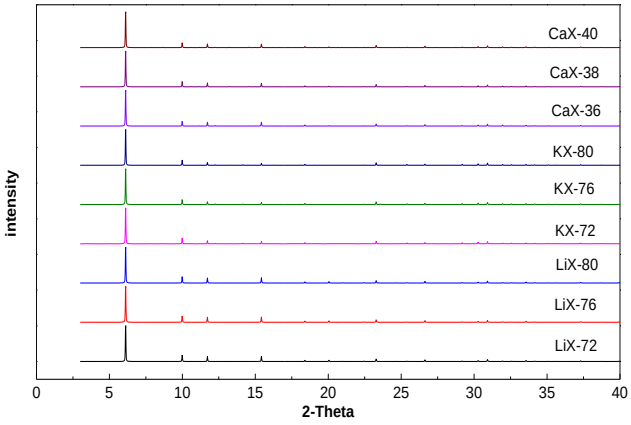

Fig.4. XRD patterns for LiX, KX, and CaX zeolites models.

3.1.2 Pore Volume

The pore volume of 13X zeolite was calculated using MS software, obtaining a value of 0.28

215 $cm^3\ g^{-1}$. To demonstrate the rationality of the model, the simulated result was compared with the
216 experimental results of Garshasbi and Lee.[53,54] The absolute error between the simulated result and
217 experimental value is only 0.03 $cm^3\ g^{-1}$, indicating that the model is valid and the pore volume
218 obtained from MS software is feasible.

219 The pore volumes of metallic cation-exchanged 13X zeolite were list in Table 4. Compared to
220 the pore volume of 13X zeolite, the pore volumes of the LiX and CaX zeolites were higher, while
221 those of KX zeolite were lower. Further, the pore volumes of the LiX zeolite are slightly larger
222 than those of the CaX zeolite. Larger pore volumes indicate that a zeolite can hold more
223 adsorbates. Therefore, the LiX zeolite exhibited the highest adsorption capacity among the 13X,
224 LiX, KX, and CaX zeolites. It can also be seen from Table 4 that the variation in pore volume
225 increases with increasing degrees of ion exchange for identical zeolite. Therefore, the LiX-80
226 zeolite has the highest pore volume of all X zeolites presented in this study.

227 **Table 4** Pore volumes of metallic cation-exchanged 13X zeolite

Zeolite	Pore volume /($cm^3\ g^{-1}$)	Zeolite	Pore volume /($cm^3\ g^{-1}$)	Zeolite	Pore volume /($cm^3\ g^{-1}$)
LiX-72	0.353	KX-72	0.151	CaX-36	0.334
LiX-76	0.359	KX-76	0.150	CaX-38	0.334
LiX-80	0.365	KX-80	0.147	CaX-40	0.338

228 **3.2 Molecular simulation of single metallic cation-exchanged 13X zeolite**

229 **3.2.1 Pure gas adsorption**

230 Pure CO_2 adsorptions to 13X, LiX, KX, and CaX zeolites were simulated at a temperature of
231 298 K and pressures ranging from 0 to 1500 kPa. The adsorption isotherms of these samples are
232 type I according to the IUPAC classifications, as plotted in Fig.5. As shown in Fig.5, the CO_2
233 adsorption capacities of LiX and CaX zeolites are higher than those of 13X zeolite, while those of
234 KX zeolite are lower. This is due to the variations in pore volume for the 13X, LiX, KX, and CaX
235 zeolites. This result agrees with the experimental result of K. S. Walton et al.[22] In this study, the
236 CO_2 adsorption capacity on the NaX zeolite with Li^+, K^+, Rb^+, and Cs^+ increased in the following
237 order: Cs < Rb < K < Na < Li.

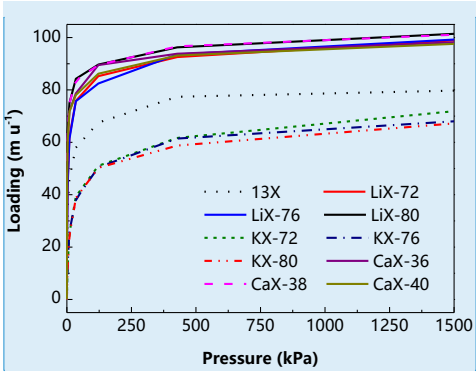

Commented [B2]: Is it possible to show unit of mmol/g or mg/g in right? It is for an comparison ofsimulation and experiments.

Fig.5. Pure CO_2 adsorption isotherms for 13X, LiX, KX, and CaX zeolites.

In the low pressure, the CO_2 adsorption capacities of all X zeolites presented in this study increased sharply. To clearly show the variation in adsorption capacity, the partial enlarged figure of Fig.5 was shown in Fig.6 (a). As shown in Fig.6 (a), Li^+ and Ca^{2+} exchanged to 13X zeolite increased obviously CO_2 adsorption capacity at low pressure. Compared to the adsorption isotherm of 13X zeolite, the adsorption isotherms of LiX and CaX zeolites shift to the left. In order to contrast with the CO_2 adsorption isotherm, pure N_2 adsorptions to 13X, LiX, KX, and CaX zeolites were simulated at a temperature of 298 K and pressures ranging from 0 to 120 kPa, as plotted in Fig.6 (b). N_2 adsorption isotherms of X zeolites exhibit nearly the same shape, which are totally different from CO_2 adsorption isotherms. It can also be observed from Fig.6 that CO_2 adsorption capacities of X zeolites are bigger than N_2 adsorption capacities at the low pressure. This is the basis of the CO_2 separation from the flue gas.

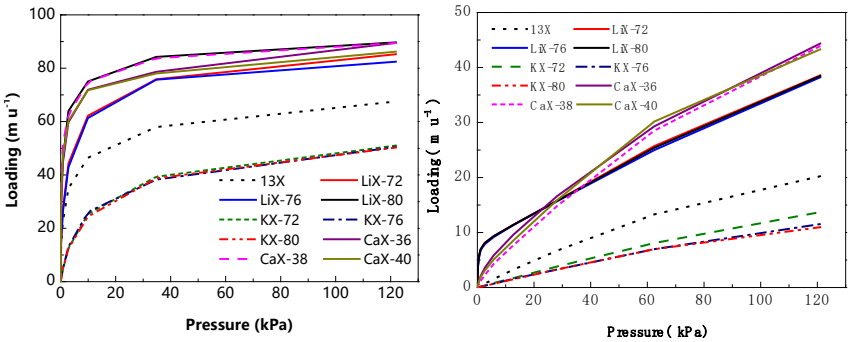

(a) CO_2 (b) N_2

Fig.6. Pure gas adsorption isotherms for 13X, LiX, KX, and CaX zeolites.

The total adsorption energy can reflect the interaction strength between adsorbent and adsorbent. The energy variation of systems (The energy refers to the sum of van der Waals energy, electrostatic energy, and intramolecular energy.) for CO_2 adsorption to the 13X, LiX, and CaX

zeolites were shown in Fig. 7. In Fig.7, the energy variation process can be divided into two stages: Above all, the average total energy decreases rapidly at initial stage because the initial CO_2 adsorption capacity of all the zeolites is very strong. Then, it becomes constant as the adsorption reaches equilibrium. Reversible physical adsorption occurs between CO_2 and the 13X, LiX, and CaX zeolites via both van der Waals interactions and electrostatic interactions. And in the GCMC simulation, van der Waals interactions between the zeolite framework and CO_2 were represented by L-J potentials, while electrostatic interactions were modeled using point charges placed on the atomic sites of the zeolites.[55] The various interaction energies at the adsorption equilibrium were listed in Table 5. It can be seen from Table 5 that LiX zeolite has the biggest van der Waals energy with CO_2. This is due to Li^+ has the smallest ionic radius. σ is the site diameter of van der Waals force, which can represent the size of the modified atom. The larger the modified atom, the bigger the space it occupies, and the smaller the free volume of CO_2 will be able to adsorb. The σ parameters of the Li, Na and Ca atoms used in the adsorption simulation are 2.451, 2.983 and 3.399 Å, respectively. Li^+ has the smallest ionic radius. Therefore, the distance is the shortest between Li^+ and the center of mass of the CO_2 molecule. Correspondingly, the LiX-80 has the biggest Van der Waals energy, as shown in Table 5. CaX zeolite has the biggest electrostatic energy with CO_2 because of the large quadrupole moment of CO_2, indicating that the Ca^{2+} may be has the biggest charge density. In general, the total energy of LiX and CaX zeolites is bigger than that of the 13X, which agrees with the results of the CO_2 loadings showed in Fig.5.

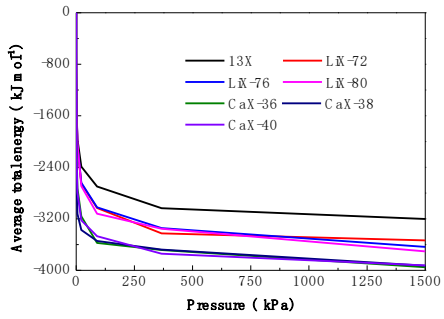

Fig.7. Energy variation of systems for CO_2 adsorption to 13X, LiX, and CaX zeolites.

Table 5 Interaction energy between X zeolite and CO_2

Energy/ (kJ mol^{-1})	13X	LiX-72	LiX-76	LiX-80	CaX-36	CaX-38	CaX-40
Van der Waals energy	-1372.15	-2073.91	-2133.48	-2193.86	-2066.11	-1876.07	-1881.80
electrostatic energy	-2005.49	-1666.35	-1718.29	-1737.50	-2097.22	-2254.71	-2246.41
Intramolecular energy	174.97	246.70	215.51	226.18	211.25	202.71	204.89
Total energy	-3202.67	-3493.56	-3636.26	-3705.18	-3952.08	-3928.07	-3923.32

The difference in the CO_2 adsorption capacity between the LiX and CaX zeolites is very small. To obtain an appropriate adsorbent, it is necessary to consider the regeneration performance.

Here, the isosteric heats for CO_2 adsorption to the 13X, LiX, and CaX zeolites were shown in Fig.8. The isosteric heat for CO_2 adsorption to LiX zeolite is 43.998~62.617 kJ mol^{-1} in Fig.8. Compared with the literature data of 50~70 kJ mol^{-1},[56] there is little difference between the simulation results and experimental results, which indicates that the simulation methods are reliable. The initial isosteric heat can indirectly reflect interactions between zeolite and gas, and it can be used as a quantitative indicator. In Fig.8, the initial isosteric heats for CO_2 adsorption to the zeolites follow the order: LiX-80>CaX-38>13X>CaX-40>CaX-36, indicating that Li^+ exchanged zeolites have the stronger interaction with CO_2. This can also explain the phenomenon that the adsorption capacities of LiX-80 and CaX-38 zeolite are higher than those of 13X zeolite, as shown in Fig.5. In the late stage of adsorption, the isosteric heat of CO_2 on LiX zeolite is minimum compared with those on 13X and CaX zeolites. According to the law of conservation of energy, the more heat released during adsorption, the more heat required for the regeneration of the X zeolite.[57] Therefore, the regeneration of LiX zeolite requires less heat compared with those of 13X and CaX zeolites.

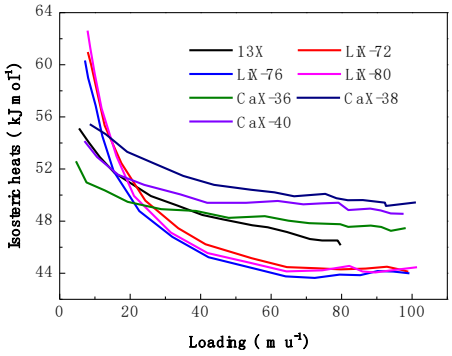

Fig.8. Isosteric heats for CO_2 adsorption to 13X, LiX, and CaX zeolites.

3.2.2 CO_2/N_2 mixture adsorption

The adsorptions of the CO_2/N_2 mixture to the 13X, LiX, and CaX zeolites at a temperature of 298 K and pressures ranging from 0 to 1500 kPa were simulated. The CO_2/N_2 selectivities of 13X, LiX, and CaX zeolite were shown in Fig.9. During the initial stage, the CO_2/N_2 selectivities of the 13X, LiX, and CaX zeolites were very high, indicating that CO_2 was almost completely adsorbed from the CO_2/N_2 mixture. As the pressure increases, the CO_2/N_2 selectivities of 13X, LiX, and CaX zeolite decreased markedly. The CO_2/N_2 selectivities of the LiX and CaX zeolites are higher than those of the 13X zeolite at the same pressure. Li^+ and Ca^{2+} have different effects on the CO_2/N_2 adsorption selectivity. The high CO_2/N_2 selectivities of the CaX zeolite is related to the strong electrostatic interactions between CO_2 and CaX zeolite, which also can be explained by the

electrostatic energy. Because the LiX-80 has the biggest van der Waals energy, it has the higher CO_2/N_2 selectivity, showing that atoms with small σ are favourable for the separation of CO_2. According to Fig.6, the adsorbed amounts of CO_2 for LiX-80 zeolite are higher than those for CaX zeolite, whereas the adsorbed amounts of N_2 for LiX-80 are lower than those for CaX. Consequently, the CO_2/N_2 selectivity of LiX-80 is the highest among all of the above zeolites.

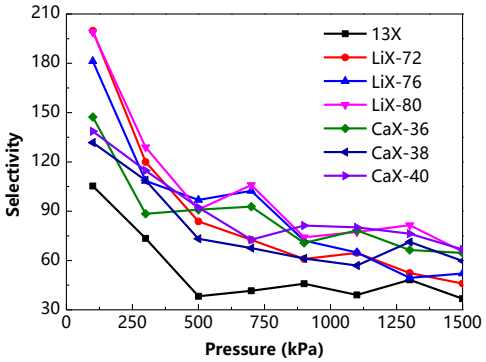

Fig.9. CO_2/N_2 selectivities of 13X, LiX, and CaX zeolites.

3.3 Molecular simulation of polymetallic cation-exchanged 13X zeolite

The maximum CO_2/N_2 selectivity of the LiX-80 zeolite at 100 kPa is 200. This value is well below the experimental result (327) obtained by Zhang using MOFs to capture CO_2 from a CO_2/N_2 mixture.[58] To obtain an appropriate adsorbent in CO_2 capturing from flue gas, the further modification of LiX zeolite was conducted. In response to the results of previous studies,[22,52-54,57,58] a small number of Pd and Ag metallic cations were exchanged into the LiX-80 zeolite; the molar ratio of Pd to Ag was 77:23. The modified zeolite containing Pd^{2+}, Ag^{+}, and Li^{+} was denoted as LiPdAgX zeolite.

3.3.1 Pure gas adsorption

Adsorption isotherms of CO_2 and N_2 adsorbed on 13X, LiX-80 and LiPdAgX zeolites at 298 K and pressures ranging from 0 to 120 kPa were presented in Fig.10. Compared to that of CO_2, the adsorption isotherm of N_2 was linear, showing the weak interaction between N_2 and zeolites. CO_2 adsorption capacities for 13X, LiX-80 and LiPdAgX zeolites were significantly higher than N_2 adsorption capacities because of its high degree of polarizability and large quadrupole moment.

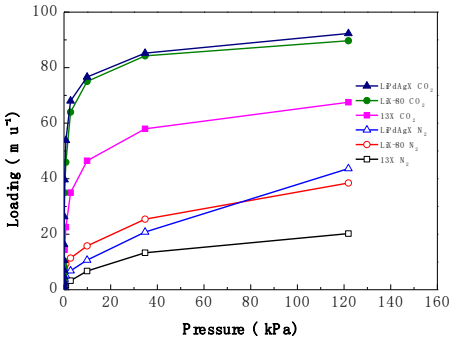

Fig.10. CO_2 and N_2 adsorption isotherms for 13X, LiX-80 and LiPdAgX zeolites.

The isosteric heats for CO_2 and N_2 adsorption to the LiX-80 and LiPdAgX zeolite were showed in Fig.11. The initial isosteric heats for CO_2 and N_2 adsorption to the LiX zeolite were respectively 66.129 and 39.838 kJ mol^{-1} that are very close to the experimental data (70 and 44 kJ mol^{-1}).[56] Compared to LiX zeolite, the initial isosteric heat for CO_2 adsorption to the LiPdAgX zeolite significantly increased from 66.129 kJ mol^{-1} to 71.794 kJ mol^{-1}, while that of N_2 exhibited little increase. This is because the quadrupole moment of CO_2 is larger than that of N_2. The interaction of the LiPdAgX zeolite with CO_2 was intense that with N_2, which is very beneficial for CO_2 capture. As the loading increased, the curve of the isosteric heats gradually decreased due to reductions in the numbers of favourable active adsorption sites.

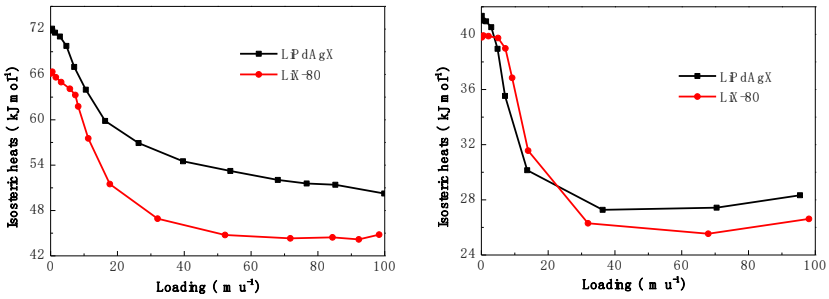

(a) CO_2 (b) N_2

Fig.11. Isosteric heats for the adsorption of (a) CO_2 and (b) N_2

3.3.2 CO_2/N_2 mixture adsorption

The adsorptions of the CO_2/N_2 mixture to the LiX-80 and LiPdAgX zeolites were simulated at a temperature of 298 K and pressures ranging from 0 to 1500 kPa . The CO_2/N_2 selectivities of LiX-80 and LiPdAgX zeolites were depicted in Fig.12. It can be seen in Fig.12 that the CO_2/N_2 selectivity of the LiPdAgX zeolite is higher than that of the LiX-80 zeolite at the same pressure, and the maximum value of the LiPdAgX zeolite is 367 at a pressure of 100 kPa. This value is

higher than the experimental result presented by Zhang using MOFs to capture CO_2 from a CO_2/N_2 mixture.[58] indicating that the LiPdAgX zeolite can capture CO_2 from CO_2/N_2 mixture more effectively than the LiX-80 zeolite.

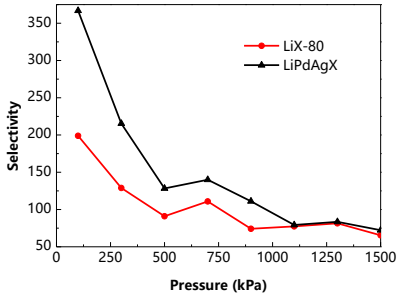

Fig.12. CO_2/N_2 selectivities of LiX-80 and LiPdAgX zeolites.

The difference in the CO_2/N_2 selectivity between the LiX-80 and LiPdAgX zeolites can be explained by the ESP of the metallic cations. The interactions between CO_2/N_2 and each zeolite include van der Waals and electrostatic forces. Due to the large quadrupole moment of the CO_2 molecule, which is nearly three times that of N_2, the adsorption of CO_2 can be improved by increasing the proportion of electrostatic forces in the total force field. Increasing the ESP of cations in a zeolite can improve the electrostatic forces between the zeolite and CO_2.

To demonstrate the validity of this interpretation, ESP calculations were performed on cluster structures cut from the LiX-80, LiPdX, LiAgX, and LiPdAgX zeolites. The only difference in the cluster structures, as observed in Fig.13 (a), is the metallic cation of the centre. The gradients of potential and the strength of the electrostatic field in the pores of the LiX-80, LiPdX, LiAgX, and LiPdAgX zeolites were compared by generating contour maps of the ESP for zeolite (Fig.13). The ESP field in the pores of the LiPdAgX zeolite appears to be stronger than those of the LiX, LiPdX, and LiAgX zeolites. It is shown that the potential around Pd ions and Ag ions is larger than Li ions, and the potential of Pd and Ag coexisting in the skeleton is higher than the electrostatic potential of each metal alone. Moreover, the electrostatic energy between the LiPdAgX zeolite and CO_2 is -2330.36 kJ mol^{-1}, which is also the highest among 13X and all modified zeolites. Therefore, the LiPdAgX zeolite has a higher CO_2/N_2 selectivity than the other modified zeolite in this study.

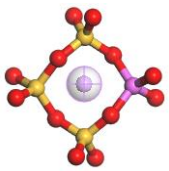

(a) Cluster structure

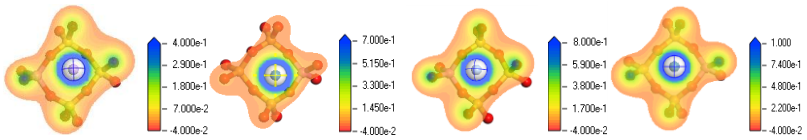

(b)LiX-80 (c) LiPdX (d) LiAgX (e) LiPdAgX

Fig.13. Cluster structure (a) and contour maps of ESP for the (b) LiX-80, (c) LiPdX, (d) LiAgX, and (e) LiPdAgX zeolites. Key: red= O; yellow= Si; purple= Al; grey= Li in (b), Pd in (c), Ag in (d), and Pd in (e).

The adsorption sites, models of gas in porous media, and selectivity of the adsorbent can all be affected by the ESP.[59] Adsorption density profiles and energy distribution curves of CO_2 to the LiX-80 and LiPdAgX zeolites at different pressures were shown in Fig.14. At a low pressure (Fig.14(a)), CO_2 was adsorbed on the pore wall surface of the LiX-80 zeolite by monolayer adsorption corresponding to one energy peak. Except for the surface adsorption, CO_2 was preferentially adsorbed to the most energetic Ag^+ and Pd^{2+} sites of the LiPdAgX zeolite. Correspondingly, there were three energy peaks for the LiPdAgX zeolite. As the pressure increased from 0.01 kPa to 0.8047 kPa, the multilayer adsorption on the pore wall occurred in both LiX-80 and LiPdAgX zeolites with the increase of CO_2 adsorption loading. At this time, the Ag^+ and Pd^{2+} sites of the LiPdAgX zeolite was saturated. Two peaks for both the LiX-80 and LiPdAgX zeolites were observed, indicating that there were two main adsorption sites which were the monolayer and multilayer adsorption site, respectively (Fig.14(b)). When the pressure increased from 0.8047 to 34.73 or 427.58 kPa, the adsorption of CO_2 was only the multilayer adsorption. The adsorption energy curves of the LiX-80 and LiPdAgX zeolites exhibited single peaks in Fig.14(c) and Fig.14(d). The small peak located at a narrow energy band in the energy curve of LiX-80 zeolite may be caused by molecular self-aggregation near the pore center. The above analysis showed that the addition of Ag^+ and Pd^{2+} could increase the adsorption sites of LiPdAgX zeolite at low pressure, which would improve the CO_2 adsorption capacity and adsorption selectivity of CO_2/N_2. As illustrated in the snapshots of the CO_2 density distributions from 0.01 to 427.58 kPa, the CO_2 adsorption density of the two zeolites increased with increasing pressure, and CO_2 is adsorbed to the faujasite cage. The adsorption density distributions under high pressure indicated that the density of CO_2 in LiPdAgX was higher than that in LiX-80 zeolite, indicating that the adsorption performance of the zeolite was improved by modification. Furthermore, the addition of Ag^+ and Pd^{2+} to LiX enabled a more homogeneous energy distribution at high pressures when compared to the single cation type zeolite, as shown in Fig.14(c) and Fig.14(d). The total adsorption energies of LiX-80 and LiPdAgX zeolites were -3705.18 and -3908.35 kJ mol^{-1}, respectively. Therefore, the LiPdAgX zeolite has a stronger interaction with CO_2 compared to LiX-80.

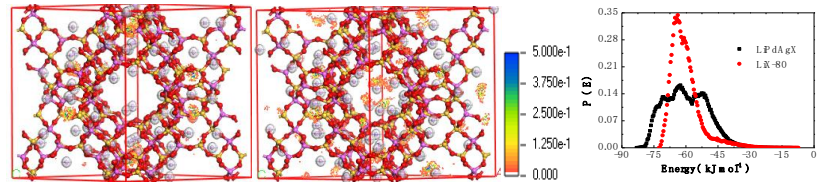

LiX-80 LiPdAgX

(a) 0.01 kPa

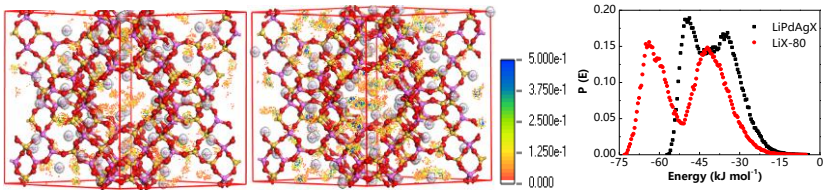

LiX-80 LiPdAgX

(b) 0.8047 kPa

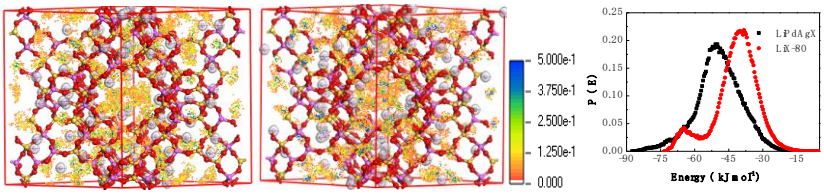

LiX-80 LiPdAgX

(c) 34.73 kPa

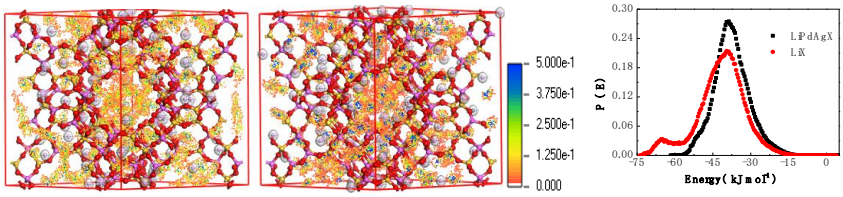

LiX-80 LiPdAgX

(d) 427.58 kPa

Fig.14. Adsorption density profiles and energy distribution curves of CO_2 to the LiX-80 and LiPdAgX zeolites at pressures of (a) 0.01 kPa, (b) 0.8047 kPa, (c) 34.73 kPa, and (d) 427.58 kPa.

The CO_2 loading at 1500 kPa, CO_2/N_2 selectivity and average isosteric heat of CO_2/N_2 mixture adsorption from 0 to 1500 kPa for 13X, LiX-80, and LiPdAgX zeolites were compared as shown in Fig.15. Compared with 13X zeolite, the CO_2 adsorption capacities of LiX-80 and LiPdAgX zeolites increased respectively by 23.33% and 25.22%, and the average CO_2/N_2 selectivity increased by 93.29% and 179.26%. At the same time, the isosteric heat of LiX-80 and

LiPdAgX zeolites increased by 3.08% and 7.79%, respectively. It can be seen from these data that the increase amplitude of CO_2 loading and CO_2/N_2 selectivity for LiPdAgX zeolite is much higher than that of isosteric heat. These results indicated that the LiPdAgX zeolite is more suitable for removing CO_2 from combustion flue gas.

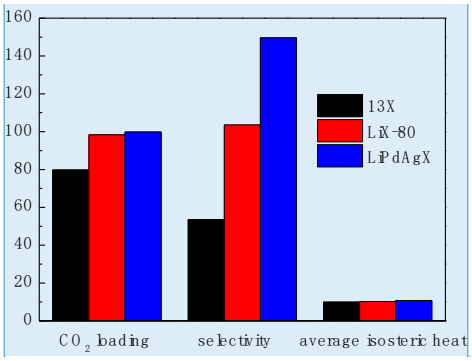

Commented [B3]: Y Unit ?

Fig.15. Comparison of the performances for the 13X, LiX-80, and LiPdAgX zeolites.

4. Adsorption experiment

4.1 Experimental materials and setup

The adsorbents used in the adsorption experiments included the 13X, LiX, and LiPdAgX zeolites. To synthesise the LiX and LiPdAgX zeolites, metal ions in salt solutions were incorporated into the 13X zeolite via ion exchange. Detailed descriptions of the synthesis of LiX and LiPdAgX zeolites are given in a previous study.[52] Based on the study, the mass ratios of $PdCl_2$ and $AgNO_3$ to 13X zeolite were 5 ‰ and 1.5 ‰, respectively. The adsorbates, CO_2 and N_2, were of high-purity (99.999% purity). An apparatus based on the volumetric method was built to measure the adsorption equilibrium data by means of the pressure drop in an adsorption tank, whose residual volume was known. The residual volume of the adsorption tank, i.e., the apparent volume subtracted by the volume occupied by the adsorbent, was determined from helium adsorption. Gas consumption was determined by measuring the decreased gas pressure. Both the pure CO_2 and CO_2/N_2 mixture were adsorbed to 13X, LiX, and LiPdAgX zeolites in the experimental apparatus of gas adsorption, as shown in Fig.16. It mainly consisted of an adsorption tank, gas chromatograph (GC), and measurement system, which has been described in detail.[60] The GC was connected to the sample connections 1, 2 and 3 at the outlet of V_3, V_8 and V_9, respectively. The GC analysis of the sample connection 1 is to obtain CO_2 content from the gas mixture before it flows into the adsorption tank. In order to improve the measure accuracy, the sample connections 2 and 3 locate at the top and bottom of the adsorption tank, respectively. The average value of CO_2 content in the gas mixture at adsorption equilibrium was got by means of

measuring the gas content of the sample connections 2 and 3, which is known as the last CO_2 content in the adsorption tank at adsorption equilibrium.

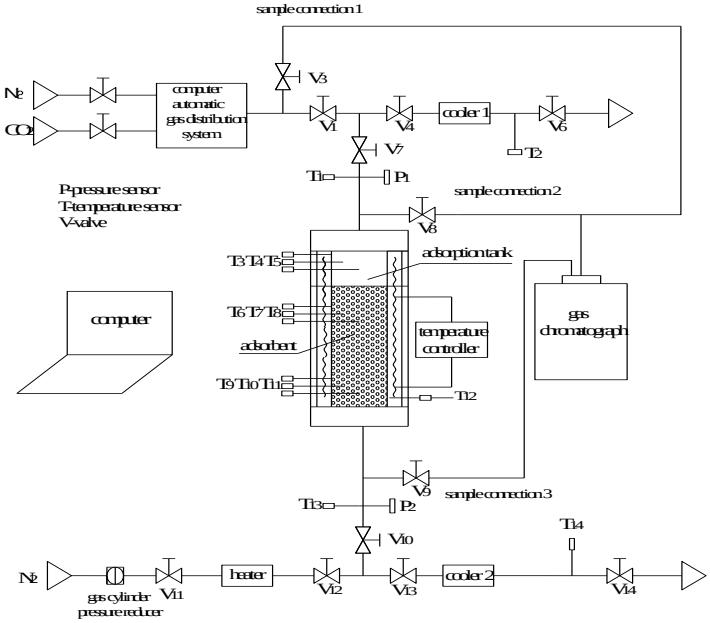

Fig.16. Experimental apparatus of gas adsorption to zeolite.

4.2 Experimental procedure

The first step is the preliminary stage of gas adsorption experiment. After activation, the 13X zeolite was fed into the adsorption tank. The adsorption tank was then heated to 473 K for 4 h by the temperature controller. 13X zeolite was pretreated to prevent contamination and moisture during the filling process. At the same time, the heated N_2 of 473 K through V_{12} and V_{10} flows the adsorption tank and all the pipes in order to ensure no moisture in the adsorbents and pipes, which also makes the gas dry. Before the pure CO_2 was adsorbed, the adsorption tank was cooled to 298 K.

In the second step of the procedure, pure CO_2 was adsorbed to the 13X zeolite at 298 K and pressures ranging from 0 to 1500 kPa. If the device was suitably airtight for the requirements of the experiment, V_1 and V_7 were opened, and pure CO_2 could flow into the adsorption tank. When the pressure of the adsorption tank reached a predetermined value, V_7 was closed, and the value was recorded. At the same time, the adsorption process started. The temperature of the adsorption tank increased rapidly then decreased slowly until 298 K during the adsorption process. The time far away from 298 K is transitory contrary to that of the adsorption process. Because the adsorption capacity is a quantity of state, the effect of the temperature variation during the

adsorption process on the measurement of the adsorption capacity is very little. In order to further reduce this influence, the increase of the thermal conductivity for the adsorbents is an inevitable trend. The adsorption equilibrium was only achieved once the pressure became constant over a period of 3 h and the temperature of the tank stabilized at 298 K. After the equilibrium was established, pure CO_2 was again allowed to flow into the adsorption tank. This procedure was repeated until the full CO_2 adsorption isotherm was obtained.

Prior to the next step measurement, the saturated 13X zeolite was activated at 473 K for regeneration. It was not until the pressure became constant within 2 h that the regeneration of 13X zeolite was realized. Afterwards, it was cooled down to 298 K. Then, the next step was CO_2/N_2 mixture adsorption experiment for 13X zeolite at a temperature of 298 K and different pressures ranging from 0 to 1500 kPa. The molar fractions of CO_2 and N_2 in the mixture were 3% and 97%, respectively. The experimental procedure of this third step was identical to that of the second step except for the adsorbate and the measurement of gas content. The adsorbate was changed from pure CO_2 to a CO_2/N_2 mixture. Before the gas mixture adsorption, the gas content at each pressure was measured by GC at the sample connection 1. When the adsorption equilibrium was realized, the gas content at equilibrium pressure was measured by GC at the sample connections 2 and 3. The pressure and temperature of the adsorption tank were recorded automatically by a computer during the gas adsorption.

The experimental procedures described above were then repeated, with the 13X zeolite being replaced by the LiX and then the LiPdAgX zeolites.

4.3 Experimental results

The experimental adsorption isotherms for pure CO_2 adsorbed in 13X, LiX, and LiPdAgX zeolites were respectively shown in Fig.17, and the corresponding lowest pressures recorded in the experimental isotherms were 30, 80, and 20 kPa. The adsorption capacity for CO_2 in the LiPdAgX zeolite was higher than that in the 13X and LiX zeolites at the same pressure, which agrees well with the simulated results. As mentioned in Section 3.3, the increase in the adsorption capacity for CO_2 in LiPdAgX is related to the improvement of both the CO_2 active adsorption site and the ESP gradient caused by the presence of Pd^{2+} and Ag^{+}. In addition, the effective release of adsorption heat by zeolites can improve their adsorption capacity. The thermal conductivity of the zeolite was measured by a HotDisk TPS2500 thermal conductivity coefficient instrument, and the thermal conductivities of zeolite were 0.1169, 0.1129, and 0.1192 W $(m\ K)^{-1}$ for the 13X, LiX, and LiPdAgX zeolites, respectively. The differences in thermal conductivity between the three zeolites might be caused by differences in the metal ions present in each material. The LiPdAgX zeolite exhibits good thermal conductivity, which is more conducive to the adsorption process.

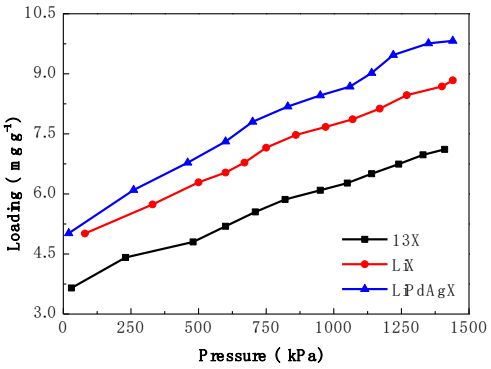

Fig.17. Pure CO_2 adsorption isotherms of zeolite.

The adsorption selectivities of CO_2/N_2 were calculated based on the results of the mixed gas adsorption experiment. The selectivity of CO_2/N_2 at 100 kPa for LiX zeolite was 283.5. This value is also less than the experimental result (327) obtained by zhang,[58] indicating that further modification of LiX zeolite is necessary in order to obtain the excellent adsorbent. To compare the adsorption selectivity of the three zeolites, four points of higher pressure were selected to calculate the adsorption selectivity, revealing that the selectivity of each zeolite decreased with increasing pressure, the result was listed in Table 6.

Table 6 Adsorption selectivities of CO_2/N_2 based on mixed gas adsorption experiment

13X		LiX		LiPdAgX	
Pressure/ kPa	selectivity	Pressure/ kPa	selectivity	Pressure/ kPa	selectivity
1060	92.0	1050	137.0	1070	240.0
1160	90.8	1160	115.7	1170	213.6
1270	92.2	1270	99.9	1260	162.7
1370	71.3	1380	102.6	1370	128.0

As can be seen from the data in the Table 6, the selectivity of the two modified zeolites were significantly higher than that of the 13X zeolite. The selectivity of LiX increased by 43.9%, to 102.6, while the same parameter for LiPdAgX improved by 79.5%, to 128.0. CO_2 adsorption capacities of 13X zeolite between the simulated and experimental results were directly compared by Fig.5 and Fig.17, LiPdAgX zeolite by Fig.10 and Fig.17. The CO_2/N_2 selectivities of for 13X zeolite between the simulated and experimental results were directly compared by Fig.9 and Table 6, LiPdAgX zeolite by Fig.12 and Table 6. It can be seen from these direct comparison that there was a quantitative difference between the experimental and simulated results of the CO_2 adsorption capacity and selectivity of CO_2/N_2. However, the order of the experimental result (13X ＜LiX＜LiPdAgX) agrees with the simulated order, indicating that the simulation could qualitatively assess the modification and adsorption performance of the zeolite. This quantitative difference may be led by the sample and the residual volume of the adsorption tank. 13X zeolite is

a pure substance of $Na_{86}Al_{86}Si_{106}O_{384}$ in the simulation. However, it is a mixed substances which comprises of $Na_{86}Al_{86}Si_{106}O_{384}$ and some agglomerants for the experimental sample. For the residual volume of the adsorption tank, there is an inevitable error due to gravity and the impact of the airflow. Before the gas adsorption experiment, the residual volume of the adsorption tank was measured, and the value was deemed to the constant during the process of gas adsorption. However, the value will increase as the experiment goes on due to gravity and the impact of the airflow. Therefore, the vertical comparison is more significance than the horizontal comparison for the simulated and experimental results. In any case, both the simulated and experimental results show that the LiPdAgX zeolite exhibits both the highest adsorption capacity and selectivity of CO_2/N_2.

On the basis of the ongoing research activities conducted so far, it appears that the adsorbent materials must satisfy some important criteria to be both economical and operational for CO_2 capture from flue gas. These criteria are as follows: the high CO_2 adsorption capacity at low pressures, high CO_2/N_2 selectivity, fast adsorption/desorption kinetics, moderate adsorbent costs, and excellent thermal, chemical, and mechanical stabilities.[31,61] These factors are all important for candidate adsorbents being developed and for the design of CO_2 separation system. Other than those data, information such as the isosteric heat, specific heats, mass-transfer and diffusional effects, and particle/bed characteristics of solid adsorbents are also essential.[61] The efficient use of LiPdAgX zeolite in a particular contactor type is a key and will ultimately determine whether the technology can indeed be economical for CO_2 capture from flue gas. There is no doubt that the addition of $PdCl_2$ to 13X zeolite will increase the cost of the absorbent, which may limit the large-scale applications of LiPdAgX zeolite. However, it is only one of influence factor for CO_2 capture cost from flue gas. Zhang et al.[62] found that the operating capture costs vary significantly with process configuration and operating parameters, such as feed gas temperature, feed concentration and evacuation pressure. Because of the lack of sufficient data on LiPdAgX zeolite performance in various contactor configurations, it is difficult to determine quantitatively the CO_2 capture cost. In previous work, our group have concluded that the capture cost per ton of CO_2 avoided using LiPdAgX zeolite is less than that using the convention monoethanol amine absorption.[52] Compared to 13X zeolite, LiPdAgX zeolite has the better CO_2 adsorption capacity and high CO_2/N_2 selectivity. Therefore, it is suitable for CO_2 capturing from flue gas.

5. Conclusion

In this study, both molecular simulation and experimental procedures were used to investigate CO_2 capture in 13X and cation-exchanged 13X zeolites. The 13X zeolite model was established and its reliability was verified by comparing the simulated XRD pattern with experimental data. Different degrees of metallic cation-exchanged zeolite models were obtained

by introducing Li^+, K^+, and Ca^{2+} to the 13X zeolite. Through molecular simulation, the pore volume, CO_2 adsorption capacity, regeneration performance and CO_2/N_2 selectivity of different cation-exchanged 13X zeolites were compared, and the results indicated that the LiX-80 zeolite exhibited the best performance. To improve its separation efficiency, small numbers of Pd^{2+} and Ag^+ were exchanged into LiX-80, creating the model LiPdAgX zeolite. Further study illustrated that the CO_2 adsorption capacity and average CO_2/N_2 selectivity of the LiPdAgX zeolite were 1.89% and 85.97% better than those of LiX-80, respectively. The increase in the CO_2/N_2 selectivity for LiPdAgX zeolite can be attributed to the gradient of potential and stronger ESP fields of Pd^{2+} and Ag^+. The adsorption sites of the LiPdAgX zeolite are affected by these ESP changes, as revealed by the adsorption density profiles and energy distribution curves.

Finally, adsorption experiments were conducted on the 13X, LiX, and LiPdAgX zeolites. The order of experimental results for 13X, LiX, and LiPdAgX zeolites about CO_2 adsorption capacity and CO_2/N_2 selectivity agrees with the simulated order, indicating that the molecular simulation approach used here is a reliable method of guiding for the design of high-performance cation-exchanged zeolite and assessing the effectiveness of zeolites for targeted separation, such as CO_2 capture. The results demonstrate that LiPdAgX is the most suitable adsorbents for removing CO_2 from flue gas, followed by LiX and 13X.

Acknowledgements

We acknowledge funding support from the National Natural Science Foundation of China (No. 51306210), the Fundamental Research Funds for the Central Universities (No. 18CX02080A) and China Scholarship Council (No. 201706455001).

References

1 R. Dawson, A. I. Cooper and D. J. Adams, *Polym. Int.*, 2013, 62, 345.
2 *Energy technology perspectives 2008*, International Energy Agency, Paris, 2008.
3 M. Wang, A. Lawal, P. Stephenson, J. Sidders and C. Ramshaw, *Chem. Eng. Res. Des.*, 2011, 89, 1609.
4 K.-M. Li, S.-C. Tian, J.-G. Jiang, J.-M. Wang, X.-J. Chen and F. Yan, *J. Mater. Chem. A*, 2016, 4, 5223.
5 F. Su and C. Lu, *Energy Environ. Sci.*, 2012, 5, 9021.
6 V. Benoit, N. Chanut, R. S. Pillai, M. Benzaqui, I. Beurroies, S. Devautour-Vinot, C. Serre, N. Steunou, G. Maurin, and P. L. Llewellyn, *J. Mater. Chem. A*, 2018, 6, 2081.
7 K. Li, J. Jiang, S. Tian, F. Yan and X. Chen, *J. Mater. Chem. A*, 2015, 3, 2166.
8 M. G. Rabbani, T. Islamoglu and H. M. El-Kaderi, *J. Mater.Chem. A*, 2017, 5, 258.
9 F. Su, C. Lu, W. Cnen, H. Bai and J. F. Hwang, *Sci. Total Environ.*, 2009, 407, 3017.
10 A. Shahtalebi, M. Mar, K. Guerin and S. K. Bhatia, *Carbon*, 2016, 96, 565.
11 J. Merel, M. Clausse and F. Meunier, *Ind. Eng. Chem. Res.*, 2008, 47, 209.
12 C.-T. Chou and C.-Y. Chen, *Sep. Purif. Technol.*, 2004, 39, 51.
13 K. T. Chue, J. N. Kim, Y. J. Yoo, S. H. Cho and R. T. Yang, *Ind. Eng. Chem. Res.*, 1995, 34, 591.
14 J. Mérel, M. Clausse and F. Meunier, *Environ. Prog.*, 2006, 25, 327.
15 O. Cheung and N. Hedin, *RSC Adv.*, 2014, 4, 14480.
16 P.D. Jadhav, R. V. Chatti, R. B. Biniwale, N. K. Labhsetwar, S. Devotta and S. S. Rayalu, *Energ Fuel*, 2007,

21, 3555.
17 T. Remy, S. A. Peter, L. V. Tendeloo, S. V. der Perre, Y. Lorgouilloux, C. E. A. Kirschhock, G. V. Baron and J. F. M. Denayer, *Langmuir*, 2013, 29, 4998.
18 J.-F. Yang, Q. Zhao, H. Xu, L.-B. Li, J.-X. Dong and J.-P. Li, *J. Chem. Eng. Data*, 2012, 57, 3701.
19 R. Krishnaa and J. M. van Baten, *Sep. Purif. Technol.*, 2018, 206, 208.
20 P. D. Ganga, K. Munusamy, S. S. Rajesh and C. B. Hari, *Indian J Chem. A*, 2012, 51, 1238.
21 T. D. Pham, Q.-L. Liu and R. F. Lobo, *Langmuir*, 2013, 29, 832.
22 K. S. Walton, M. B. Abney and M. D. LeVan, *Micropor. Mesopor. Mater.*, 2006, 91, 78.
23 R. S. Pillai, S. A. Peter and R. V. Jasra, *Micropor. Mesopor. Mater.*, 2012, 162, 143.
24 O. Cheung, Z. Bacsik, P. Krokidas, A. Mace, A. Laaksonen and N. Hedin, *Langmuir*, 2014, 30, 9682.
25 J. L. Carter, D. J. C. Yates, P. J. Lucchesi, J. J. Elliott and V. Kevorkian, *J. Phys. Chem.*, 1966, 70, 1126.
26 R.-T. Yang and E. S. Kikkinides, *AICHE J.*, 1995, 41, 509.
27 N. Chen and R.-T. Yang, *Ind. Eng. Chem. Res.*, 1996, 35, 4020.
28 R.-T. Yang, Y.-D. Chen, J.-D. Peck and N. Chen, *Ind. Eng. Chem. Res.*, 1996, 35, 3093.
29 T. Frising and P. Leflaive, *Micropor. Mesopor. Mater.*, 2008, 114 , 27.
30 O. Terekhina and E. Roduner, *J. Phys. Chem. C*, 2012, 116, 6973.
31 Z.-N. Song, Q.-B. Dong, W.-W. L. Xu, F.-L. Zhou, X.-H. Liang and M. Yu, *ACS Appl. Mater. Interfaces*, 2018, 10, 769.
32 K. T. Leperi, R. Q. Snurr and F. You, *Ind. Eng. Chem. Res.*, 2016, 55, 3338.
33 C. E. Wilmer, M. Leaf, C. Y. Lee, O. K. Farha, B. G. Hauser, J. T. Hupp and R. Q. Snurr, *Nat. Chem.*, 2012, 4, 83.
34 J. Kim, M. Abouelnasr, L.-C. Lin and B.Smit, *J. Am. Chem. Soc.*, 2013, 135, 7545.
35 K. Zhang, A. Nalaparaju and J.-W. Jiang, *J. Mater. Chem. A*, 2015, 3, 16327.
36 Y.-Y. Liu and J. Wilcox, *Environ. Sci. Technol.*, 2013, 47, 95.
37 R. Babarao and J. W. Jiang, *Ind. Eng. Chem. Res.*, 2011, 50, 62.
38 R. S. Pillai, G. Sethia and R. V. Jasra, *Ind. Eng. Chem. Res.*, 2010, 49, 5816.
39 M. K. Crawford, K. D. Dobbs, R. J. Smalley, D. R. Corbin, N. Maliszewskyj, T. J. Udovic, R. R. Cavanagh, J. J. Rush and C. P. Grey, *J. Phys. Chem. B*, 1999, 103, 431.
40 S.-J. Chen, Y. Fu, Y.-H. Huang, Z.-C. Tao, *J Porous Mat.*, 2016, 23, 713.
41 H. Panezai, J.-H. Sun, X.-Q. Jin and R. Ullah, *Sep. Purif. Technol.*, 2018, 197, 418.
42 D. Newsome, S. Gunawan, G. Baron, J. Denayer and M.-O. Coppens, *Adsorption*, 2014, 20, 157.
43 S. Sircar, *Ind. Eng. Chem. Res.*, 2006, 45, 5435.
44 J. J. Potoff and J. I. Siepmann, *AIChE J*, 2001, 47, 1676.
45 G. Maurin, P. L. Llewellyn and R. G. Bell, *J. Phys. Chem. B*, 2005, 109, 16084.
46 D. Smykowski, B. Szyja and J. Szczygieł, *J. Mol. Graph. Model.*, 2014, 50, 35.
47 M. H.Ghatee and H. Karimi, *J. Mol. Liq.*, 2013, 181,14.
48 H.-J. Fang, H. Demir, P. Kamakoti and D. S. Sholl, *J. Mater. Chem. A*, 2014, 2, 274.
49 D.-F. Liu, Y.-B. Wu, Q.-B. Xia, Z. Li and H.-X. Xi, *Adsorption*, 2013, 19, 25.
50 A.D. Corso, A. Pasquarello and A. Baldereschi, *Phys. Rev. B*, 1996, 53, 1180.
51 L.-H. He, F. Liu, G. Hautier, M. J. T. Oliveira, M. A. L. Marques, F. D. Vila, J. J. Rehr, G.-M. Rignanese and A.-H. Zhou, *Phys. Rev. B*, 2014, 89, 064305-1.
52 S.-J. Chen, M. Zhu, Y. Fu, Y.-X. Huang, Z.-C. Tao and W.-L. Li, *Appl. Energy*, 2017, 191, 87.
53 V. Garshasbi, M. Jahangiri and M. Anbia, *Appl. Surf. Sci.*, 2016, 393, 225.
54 J. S. Lee, J. H. Kim, J. T. Kim, J. K. Suh, J. M. Lee and C. H. Lee, *J. Chem. Eng. Data.*, 2002, 47, 1237.
55 M. Fischer and R. G. Bell, *J. Phys. Chem. C*, 2012, 116, 26449.
56 Y. Park, D.-K. Moon, Y.-H. Kim, H. Ahn and C.-H. Lee, *Adsorption*, 2014, 20, 631.
57 W.-B. Zhang, H. Liu, Y. Sun, J. Cakstins, C.-G. Sun and C. E. Snape, *Appl. Energy*, 2016, 168, 394.
58 Z.-J. Zhang, Y.-G. Zhao, Q.-H. Gong, Z. Li and J. Li, *Chem. Commun.*, 2013, 49, 653.
59 Q.-Y. Yang and C.-L. Zhong, *J. Phys. Chem. B*, 2006, 110, 17776.
60 S.-J. Chen, Y. Fu, Y.-X. Huang, Z.-C. Tao and M. Zhu, *Appl. Energy*, 2016, 179, 329.
61 A. Samanta, A. Zhao, G. K. H. Shimizu, P. Sarkar and R. Gupta, *Ind. Eng. Chem. Res.*, 2012, 51, 1438.
62 J. Zhang, P.A. Webley and P. Xiao, *Energy Convers. Manage.*, 2008, 49, 346.
584